INTERNATIONAL JOURNAL FOR NUMERICAL METHODS IN FLUIDS
Int. J. Numer. Meth. Fluids 2007; **55**:455–482
Published online 14 March 2007 in Wiley InterScience (www.interscience.wiley.com). DOI: 10.1002/fld.1463

Multi-resolution implicit large eddy simulations using a high-order overset-grid approach‡

S. E. Sherer*, † and M. R. Visbal

Air Vehicles Directorate, Air Force Research Laboratory, Wright-Patterson Air Force Base, OH, U.S.A.

SUMMARY

A parallel, high-order, overset-grid method is validated for use in large eddy simulation (LES) through its application to fundamental turbulent flow problems. The current method employs a high-order, compact finite-difference approach to evaluate spatial derivatives, with up to tenth-order low-pass filters used to remove high-frequency spurious wave content. These filters have also been found to be effective in modelling the dissipation that occurs at the unresolved scales in the flow for LES simulations. Temporal integration is based on an implicit, approximately factored and diagonalized, second-order algorithm, which reduces the time-step constraints present in explicit time-marching methods for wall-bounded viscous flows. Parallelization, geometric complexity, and local grid refinement are all addressed through the use of an overset-grid approach, with grid communication provided by high-order Lagrangian interpolation. The problems investigated in this work include fully turbulent channel flow at $Re_\tau = 590$ and 1017, and the transitional wake generated by flow over a single circular cylinder at $Re_D = 3900$. The results obtained with the current approach are validated against well-resolved benchmark calculations or experiments and the impact of the order-of-accuracy of the interpolation method is investigated. The benefits obtained by using the general overset-grid technique to reduce grid point requirements compared to single-grid simulations are also examined. It is shown that for the problems considered in this work, substantial grid-point savings may be obtained with an overset-grid approach compared to a single-grid approach, and that the use of high-order interpolation at overset boundaries is important in maintaining overall solution accuracy. Published in 2007 by John Wiley & Sons, Ltd.

Received 8 March 2006; Revised 18 January 2007; Accepted 20 January 2007

KEY WORDS: high-order methods; overset grid methods; turbulence; computational fluid dynamics

*Correspondence to: S. E. Sherer, Rm 225 Bldg 146, 2210 Eighth Street, Wright-Patterson AFB, OH 45433, U.S.A.
†E-mail: scott.sherer@wpafb.af.mil

Contract/grant sponsor: Air Force Office of Scientific Research
Contract/grant sponsor: Aeronautical Systems Center

1. INTRODUCTION

Direct numerical simulation (DNS) and large eddy simulation (LES) have developed into valuable tools for the investigation of fundamental turbulent fluid flows. DNS, which resolves all important turbulent scales in the flow, has been successfully employed for problems involving lower Reynolds numbers and simple geometries. DNS techniques have proven useful in the study of the development and transition of turbulent flows, but are currently not feasible for higher Reynolds numbers due to the computational costs involved in resolving all turbulent scales. For these more demanding situations, LES has been effectively used as an alternative to DNS. By resolving the larger turbulent structures while modelling the smallest, typically homogeneous, turbulent scales, LES allows for the simulation of higher Reynolds number turbulent flows than may be accomplished using DNS with current computational resources.

Because of their ability to resolve smaller scales for a given grid resolution, high-order spatial algorithms are attractive for use in DNS and LES. Examples of such methods employed in DNS and LES computations include compact finite-differences [1–3], spectral methods [4, 5], and B-spline algorithms [6, 7]. While spectral methods possess superior accuracy, traditionally, they have been limited to simple geometries and boundary conditions due to the global character of their basis functions (although work continues on spectral-element [8] and spectral-volume [9] methods to address this issue). Both B-spline and compact finite-difference approaches possess 'spectral-like' resolution, though compact finite-difference schemes were found to have somewhat better resolution properties in general than B-spline methods [10]. Both methods allow for more complex geometries and boundary conditions to be addressed. In the B-spline formulation, this is done through the use of non-uniform meshes and zonal grid embedding [11]. In the compact finite-difference approach, overset-grid techniques [12] involving general, three-dimensional, curvilinear grids are used in conjunction with grid transformation metrics that are both high-order and geometric conservation law (GCL) enforcing [13].

Here, the focus will be on a high-order compact Padé-type compact finite-difference algorithm as implemented by Visbal and Gaitonde [14, 15]. This algorithm has been successfully parallelized using an overset-grid approach where all overlapping regions contain coincident grid points, [3] and extended [16] to the general overset situation where grid points are non-coincident in the overlap region through the use of high-order Lagrangian interpolation. In Reference [16], the high-order overset-grid approach was applied to various benchmark problems involving acoustic wave propagation as well as laminar fluid flow. In the current work, this approach is examined for use in LES by applying the algorithm to two fundamental problems of turbulent fluid flow: fully turbulent flow in a rectangular channel and transitional flow over a single circular cylinder. These problems have been previously examined [3] on single-grid topologies using the current high-order differencing/filtering algorithm. However, the ability to utilize the overset-grid concept of hole-cutting as well as maintaining high-order accuracy at non-coincident interpolation boundaries not only has the potential to permit application of the approach to more complex geometries, but also can be used to distribute grid points more efficiently than in a single-grid topology.

The remainder of the current work is broken down in the following manner. Section 2 introduces the form of the governing Navier–Stokes equations that are to be solved by the current algorithm. Section 3 addresses the various aspects of this algorithm, including the high-order formulation for calculating spatial derivatives, the high-order filtering formulas used to remove spurious high-frequency waves, the overset-grid approach, and the temporal integration equations. Section 4 details the results of the application of the algorithm on fully turbulent channel flow at $Re_\tau = 590$

Published in 2007 by John Wiley & Sons, Ltd. *Int. J. Numer. Meth. Fluids* 2007; **55**:455–482
DOI: 10.1002/fld

and 1017, and the transitional flow over a single circular cylinder at $Re_D = 3900$. Current results are compared to well-resolved DNS calculations, experimental data, and single-grid calculations to validate the high-order overset-grid approach for LES.

2. GOVERNING EQUATIONS

For all of the turbulent flow problems considered here, the governing equations are given by the three-dimensional, unfiltered, unsteady, compressible Navier–Stokes equations. When normalized by the reference quantities density (ρ_∞), velocity (u_∞), viscosity (μ_∞), and length scale (L), and with the pressure normalized by $\rho_\infty u_\infty^2$, this set of equations may be written in strong conservation form for a general, time-invariant, curvilinear coordinate system (ξ, η, ζ) as [17]

$$\frac{\partial}{\partial t}\left(\frac{\mathbf{Q}}{J}\right) + \frac{\partial \hat{F}_I}{\partial \xi} + \frac{\partial \hat{G}_I}{\partial \eta} + \frac{\partial \hat{H}_I}{\partial \zeta} = \frac{1}{Re}\left[\frac{\partial \hat{F}_v}{\partial \xi} + \frac{\partial \hat{G}_v}{\partial \eta} + \frac{\partial \hat{H}_v}{\partial \zeta}\right] \tag{1}$$

where Re is the Reynolds number and J is the Jacobian of the transformation between physical (x, y, z) space and computational (ξ, η, ζ) space, $J = \partial(\xi, \eta, \zeta)/\partial(x, y, z)$. The solution vector in the above equation is given by $\mathbf{Q} = \{\rho, \rho u, \rho v, \rho w, \rho E_t\}^T$, where ρ is the fluid density, u, v, w are the component fluid velocities, and E_t is the total energy. The inviscid and viscous flux vectors are defined as

$$\hat{F}_I = \frac{1}{J}\begin{bmatrix} \rho U \\ \rho u U + \xi_x p \\ \rho v U + \xi_y p \\ \rho w U + \xi_z p \\ \rho E_t U + p U \end{bmatrix}, \quad \hat{G}_I = \frac{1}{J}\begin{bmatrix} \rho V \\ \rho u V + \eta_x p \\ \rho v V + \eta_y p \\ \rho w V + \eta_z p \\ \rho E_t V + p V \end{bmatrix}, \quad \hat{H}_I = \frac{1}{J}\begin{bmatrix} \rho W \\ \rho u W + \zeta_x p \\ \rho v W + \zeta_y p \\ \rho w W + \zeta_z p \\ \rho E_t W + p W \end{bmatrix} \tag{2}$$

and

$$\hat{F}_v = \frac{1}{J}\begin{bmatrix} 0 \\ \xi_{x_i}\tau_{i1} \\ \xi_{x_i}\tau_{i2} \\ \xi_{x_i}\tau_{i3} \\ \xi_{x_i} b_i \end{bmatrix}, \quad \hat{G}_v = \frac{1}{J}\begin{bmatrix} 0 \\ \eta_{x_i}\tau_{i1} \\ \eta_{x_i}\tau_{i2} \\ \eta_{x_i}\tau_{i3} \\ \eta_{x_i} b_i \end{bmatrix}, \quad \hat{H}_v = \frac{1}{J}\begin{bmatrix} 0 \\ \zeta_{x_i}\tau_{i1} \\ \zeta_{x_i}\tau_{i2} \\ \zeta_{x_i}\tau_{i3} \\ \zeta_{x_i} b_i \end{bmatrix} \tag{3}$$

where p is the static pressure, the metric terms defined by $\xi_x = \partial\xi/\partial x$ (with similar definitions for the other metric quantities), and the standard summation convention of summing over repeated indices is employed. With x_i and ξ_i, $i = 1, 2, 3$ used to represent (x, y, z) and (ξ, η, ζ), respectively, the stress tensor and heat flux vector may be written as

$$\tau_{ij} = \mu\left(\frac{\partial \xi_k}{\partial x_j}\frac{\partial u_i}{\partial \xi_k} + \frac{\partial \xi_k}{\partial x_i}\frac{\partial u_j}{\partial \xi_k} - \frac{2}{3}\delta_{ij}\frac{\partial \xi_l}{\partial x_k}\frac{\partial u_k}{\partial \xi_l}\right) \tag{4}$$

Published in 2007 by John Wiley & Sons, Ltd. *Int. J. Numer. Meth. Fluids* 2007; **55**:455–482
DOI: 10.1002/fld

and

$$b_i = u_j \tau_{ij} + \frac{k}{(\gamma - 1)\mu M_\infty^2 Pr} \frac{\partial \xi_l}{\partial x_i} \frac{\partial T}{\partial \xi_l} \tag{5}$$

The contravariant velocity components and total energy are written as

$$\begin{aligned} U &= \xi_x u + \xi_y v + \xi_z w \\ V &= \eta_x u + \eta_y v + \eta_z w \\ W &= \zeta_x u + \zeta_y v + \zeta_z w \end{aligned} \tag{6}$$

and

$$E_t = \frac{T}{\gamma(\gamma - 1)M_\infty^2} + \frac{1}{2}(u^2 + v^2 + w^2) \tag{7}$$

respectively. The equation of state for a perfect gas is employed, as is Sutherland's law for the molecular viscosity μ. A constant Prandtl number of $Pr = 0.72$ is also assumed.

In standard compressible LES, the governing equations are filtered using a grid-filtering function and Favre-averaged variables are introduced. Additional subgrid-scale stress (SGS) and heat flux models are then introduced to capture the turbulent behaviour of the scales not resolved by the computational grid. In this work, however, an alternative approach is taken where the energy present at the poorly resolved, smallest scales of the flow is dissipated through the use of a high-order, low-pass, implicit spatial filter [1, 18]. Thus, no additional subgrid stress or heat flux terms are added to the governing equations. This filtering approach has been re-interpreted in the context of an Approximate Deconvolution Model [19] in Reference [20]. This filtered approach has more accurately predicted the decay of isotropic turbulence compared to the standard dynamic SGS model [21], and has shown to produce nearly identical results on wall-bounded turbulent flows at half the cost of the dynamic model [1]. Although the filter is applied explicitly to the evolving solution, this approach will be referred to as an implicit LES (ILES) method due to the fact that the application of the spatial filter is a fundamental component of the algorithm required to maintain stability by removing high-frequency, spurious numerical oscillations. Details on the spatial filter are given in the following section.

3. NUMERICAL PROCEDURE

3.1. Spatial differencing formulas

The set of equations in Equation (1) is discretized using a finite-difference approach based on the Padé-type compact finite-difference formulations of Lele [22] as implemented by Visbal and Gaitonde [14, 15, 17]. On the interior of the computational domain, the spatial derivative ϕ' of any scalar quantity ϕ may be found at the node points in computational space by solving the tridiagonal system arising from the formula

$$\Gamma \phi'_{i-1} + \phi'_i + \Gamma \phi'_{i+1} = b\frac{\phi_{i+2} - \phi_{i-2}}{4} + a\frac{\phi_{i+1} - \phi_{i-1}}{2} \tag{8}$$

The coefficients Γ, a and b in Equation (8) determine the spatial order-of-accuracy of the first derivatives as well as whether they are found in an explicit or implicit manner. In this work, the implicit interior scheme used to calculate first-order derivatives is a compact, five-point, sixth-order scheme with $\Gamma = \frac{1}{3}$, $a = \frac{14}{9}$, and $b = \frac{1}{9}$. For points located on or one point away from computational boundaries, the five-point centred formula given by Equation (8) cannot be applied and high-order one-sided formulations are utilized at these points to maintain at least fourth-order accuracy. More detail regarding these boundary formulations may found in Reference [17].

The derivatives of the inviscid fluxes are found by first calculating the fluxes at the nodes, and then differentiating each component *via* application of Equation (8). For the viscous terms, the primitive variables u, v, w, and T are differentiated using Equation (8) to form the components of the stress tensor and heat flux vector at each node. These values are then used to form the viscous flux vectors, and each component is then differentiated using the same differencing method to find the derivatives of the viscous flux vectors at the nodes.

3.2. Filtering formulas

Because the schemes generated by Equation (8) are centred, they are non-dissipative in nature. Thus, numerical instabilities arising from poor grid quality, unresolved scales, or boundary conditions will be left to grow unchecked and can potentially corrupt the solution. For this reason, a low-pass symmetric filter of the form

$$\alpha_f \hat{\phi}_{i-1} + \hat{\phi}_i + \alpha_f \hat{\phi}_{i+1} = \sum_{n=0}^{N} \frac{a_n}{2}(\phi_{i+n} + \phi_{i-n}) \tag{9}$$

is applied on the interior of the domain in each of the three coordinate directions to the primitive flow variables after every subiteration (both before and after interpolation) to remove spurious high-frequency waves and maintain solution integrity. With the constraints specified in Reference [22], a filter of the form given in Equation (9) may possess a formal order-of-accuracy of up to tenth-order through the proper selection of the coefficients a_n to eliminate terms in the truncation error. The coefficient α_f is a free parameter in the range $-0.5 < \alpha_f \leqslant 0.5$ that may be used to control the spectral response of the filter [14, 17] as well as whether the filter will be implicit ($\alpha_f \neq 0$, resulting in a tridiagonal system of equations) or explicit ($\alpha_f = 0$). As the value of α_f decreases from its maximum permissible value of 0.5 (where no filtering takes place), more energy content is removed over a wider range of wave number. The value of the coefficients $\{a_0, a_1, \ldots, a_N\}$ for centred filters of various orders-of-accuracy are given in [17] as a function of α_f. Because of the symmetric form of Equation (9) and the fact that they are being employed on the uniform mesh of computational space, the interior filters are non-dispersive, do not amplify waves at any wave number, and result in the complete annihilation of the odd-even mode.

A tenth-order centred filter represented by Equation (9) requires an 11-point stencil, and thus cannot be applied at nodes within five points of a computational boundary. At these points, a centred stencil may be retained at the cost of reducing the order-of-accuracy of the filter as the boundary is approached or higher-order one-sided filter formulations may be employed. The former approach was found to provide satisfactory results [14] for a variety of single-grid problems through the judicious use of grid clustering near boundaries. However, this approach is unacceptable when using a domain-decomposition approach to provide parallel-processing capability due to the appearance of computational boundaries in areas of the domain that would not otherwise be refined. The technique of employing one-sided, high-order filters near boundaries was proven effective for

maintaining solution integrity in various multiple-grid problems [3, 15, 23] and will be used here. The formulations for the various orders-of-accuracy of the one-sided, Padé-type filters are also given in [15] as a function of α_f.

Unlike the interior centred filters, application of the one-sided boundary filters results in the undesirable feature that waves at certain ranges of wave numbers will be amplified. For near-boundary filters, the peak amplification levels become larger as the order of the boundary filter is increased (i.e. the filter becomes more one-sided). However, the region over which this amplification occurs shifts to higher wave numbers with the order of the one-sided filter, thus improving the spectral behaviour of the filter in the well-resolved region of wave space where the scaled wave number is less than approximately 1.0. Any spurious waves that are amplified by the high-order one-sided filters in this wave space range will tend to be removed by the interior filter as they propagate away from the boundary. If the numerical stability associated with the one-sided boundary filters is an issue, the peak amplification values may also be decreased by increasing the value of the filter coefficient α_f at the points near the boundary [15, 24].

3.3. Overset methodology

An overset-grid approach [12] is utilized to provide flexibility for modelling complex geometries. It also serves as a domain-decomposition mechanism for application of the high-order approach on massively parallel computing platforms [3]. The first step in this method is to generate overset structured grids based on the physical geometry of the problem. Typically, these consist of individual body-fitted grids around each geometric feature of interest and a background grid in which the body-fitted grids are embedded. Additional grids can be included to provide better resolution in key areas or for other specific purposes. In general, the points in the overlapping regions between grid components are non-coincident and must be updated using an interpolation procedure.

Once the grids are established based on the physical requirements of the problem, they are decomposed in an overset manner for parallel implementation using the MPI communications library. For notational purposes, the grid elements generated due to geometric or resolution requirements are referred to as 'grids', while elements resulting from the decomposition of grids for parallel processing are referred to as 'blocks'. While the boundaries between grids generally consist of non-coincident grid points that are updated through an interpolation process, communication between blocks is handled though finite-sized overlaps consisting of coincident grid points. Thus, no interpolation is required *per se* at block boundaries, as data are exchanged directly between coincident points as needed. Based on previous studies [15], five-point overlap regions between blocks on the same grid are sufficient to recover the interior high-order differencing and filtering of the original non-decomposed algorithm. This five-point overlap between two adjacent blocks consists of two levels of coincident donor–receiver pairs on each side of the overlap (a 'two-point fringe' in overset-grid terminology) with a non-communicating coincident point in the middle (see Reference [15] for additional details). The number of processors available for the particular problem, the amount of memory available on each processor, and load balancing concerns all drive the decomposition of grids into blocks, with each block currently assigned to a single, unique processor. This methodology has been shown to maintain a parallel efficiency of 90% for at least up to 64 processors [25].

Once created, the connectivity between all grids and blocks that make up the computational domain is established using the spatially second-order accurate PEGASUS Version 5 software [26]. High-order interpolation offsets and interpolation coefficients are calculated as a preprocessing step

using the second-order values provided by PEGASUS as input. These high-order values are used in a general, three-dimensional, explicit interpolation formula

$$\bar{\phi}_p = \sum_{i,j,k=0}^{\sigma-1} R_k^{\zeta}(\Delta_\zeta) \cdot R_j^{\eta}(\Delta_\eta) \cdot R_i^{\xi}(\Delta_\xi) \cdot \phi_{I_p+i, J_p+j, K_p+k} \tag{10}$$

that yields the interpolated primitive flowfield variable $\bar{\phi}_p$ at an interpolation point p using the known functional values ϕ at a set of donating stencil points based on the donor point (I_p, J_p, K_p). The interpolation offsets, given by $(\Delta_\xi, \Delta_\eta, \Delta_\zeta)$, represent the distance from the base donor point (I_p, J_p, K_p) to the interpolation point in the computational space of the donor grid. The parameter σ is the formal order-of-accuracy of the interpolation method and also equals the number of stencil points in each coordinate direction. The interpolation coefficients are found from the analytical expression

$$R_n^x = \frac{(-1)^{\sigma+n-1}}{[\sigma-(n-1)!]n!} \prod_{\substack{i=0 \\ i\neq j}}^{\sigma-1} (\Delta_x - i) \tag{11}$$

Hole-cutting, or blanking, is incorporated into the algorithm by decoupling the points located inside a hole from the field points outside of the hold in the implicit spatial algorithm. Then, the centred differencing and filtering formulations are replaced with their appropriate one-sided counterparts at the hole boundaries [16].

3.4. Temporal integration

The high-order overset-grid solver uses either an implicit, second-order, approximately factored Beam-Warming method [27] or an explicit, fourth-order Runge–Kutta method implemented in low-storage form [28] to advance the solution in time. As the problems considered in this work involve simulation of viscous, wall-bounded flows using significant grid clustering, only the implicit solver was employed. In delta-form, this method may be expressed as

$$\begin{aligned}
&\left[I + \phi^i \Delta t \delta_\xi^{(2)} \left(\frac{\partial \hat{F}_I^p}{\partial \mathbf{Q}} - \frac{1}{Re}\frac{\partial \hat{F}_v^p}{\partial \mathbf{Q}}\right)\right]\left[I + \phi^i \Delta t \delta_\eta^{(2)} \left(\frac{\partial \hat{G}_I^p}{\partial \mathbf{Q}} - \frac{1}{Re}\frac{\partial \hat{G}_v^p}{\partial \mathbf{Q}}\right)\right] \\
&\quad \times \left[I + \phi^i \Delta t \delta_\zeta^{(2)} \left(\frac{\partial \hat{H}_I^p}{\partial \mathbf{Q}} - \frac{1}{Re}\frac{\partial \hat{H}_v^p}{\partial \mathbf{Q}}\right)\right] \Delta \mathbf{Q} \\
&= -\phi^i \Delta t \left[\frac{(1+\phi)\mathbf{Q}^p - (1+2\phi)\mathbf{Q}^n + \phi \mathbf{Q}^{n-1}}{\Delta t}\right] \\
&\quad -\phi^i \Delta t \left[\delta_\xi \left(\hat{F}_I^p - \frac{1}{Re}\hat{F}_v^p\right) + \delta_\eta \left(\hat{G}_I^p - \frac{1}{Re}\hat{G}_v^p\right) + \delta_\zeta \left(\hat{H}_I^p - \frac{1}{Re}\hat{H}_v^p\right)\right]
\end{aligned} \tag{12}$$

where $\phi^i = 1/(1+\phi)$, with $\phi = 0$ and $\phi = \frac{1}{2}$ for the Euler implicit and second-order, three-point backward schemes, respectively, and $\delta(\xi, \eta, \zeta)$ is the spatial differencing operator (second-order

on the left-hand side and high order on the right-hand side). The diagonalized form [29] of the approximately factored scheme is employed to improve efficiency. Newton-like subiterations [30] are employed to maintain temporal accuracy and reduce error arising from linearization, factorization, diagonalization and explicit implementation of boundary conditions at both physical and computational domain boundaries. The subiteration level in Equation (12) is referenced by the superscript p, with $\Delta\mathbf{Q} = \mathbf{Q}^{p+1} - \mathbf{Q}^{p}$, $\mathbf{Q}^{p} = \mathbf{Q}^{n}$ at $p = 1$, and $\mathbf{Q}^{p} = \mathbf{Q}^{n+1}$ as $p \to \infty$. The implicit portion of the algorithm uses second-order centred finite differencing for the spatial derivatives indicated by the $\delta^{(2)}$ operator notation. The spatial derivatives on the right-hand side of Equation (12) are evaluated using centred finite differences calculated in each coordinate direction with Equation (8), indicated by the δ operator. Nonlinear second- and fourth-order artificial dissipation terms are added to the implicit operator only in Equation (12) for stability purposes. However, the use of subiterations severely reduces the impact of the implicit damping on the solution as well as the degradation due to the use of low-order spatial derivatives in the implicit operators.

4. RESULTS

4.1. Turbulent channel flow

The first problem considered here using the high-order overset-grid algorithm is the fully developed, turbulent, incompressible ($M_\infty = 0.1$) flow through a rectangular channel. DNS and LES solutions using a variety of SGS models and solver algorithms have been previously computed for this problem at a wide range of Reynolds numbers (see for example [5, 6, 31, 32]). Channel-flow simulations at values of $Re_\tau = 180$ and 395 (based on the friction velocity u_τ and channel half-height δ) have been performed using an earlier single-grid, single-block vector implementation [33] of the previously described high-order compact algorithm with spatial filtering, and a single-grid, multiple-block parallel implementation of the algorithm [3]. In addition, channel-flow simulations at $Re_\tau = 590$ were performed using a single-grid, multiple-block topology with no SGS model (ILES) in [18]. Because of the recent implementation of high-order interpolation into the current approach, multiple-grid topologies may now be considered where the boundary points in overlapping regions between grids are not necessarily coincident.

Four primary sources of numerical error have been identified in the presence of computational boundaries for the high-order overset-grid approach. They are: (1) the use of one-sided formulations for the spatial differencing and filtering operations near boundaries; (2) error associate with accuracy of the interpolation process; (3) the discrepancy in cell volumes between grids in the overlap region; and (4) loss of resolution when going from one grid to another. The first of these issues applies at both grid and block interfaces, while the last three apply only at grid interfaces. The final two items above are somewhat related, but it is possible to decouple them; i.e. two overlapping grids can have sufficient resolution but still have a large jump in cell volumes between them (in which case one grid is over-resolved). Besides validating the current algorithm for LES, the goals of studying turbulent channel flow are two-fold: to examine the impact that the last three sources of error listed above have on the accuracy of the simulations (variations in the one-sided formulations will not be considered here); and to determine the potential for grid point savings through the application of a multi-resolution approach using nested overset grids to tailor the resolution based on the proximity to the wall.

Table I. Grid parameters for single and multiple-grid topologies for channel-flow simulation at $Re_\tau = 590$ and 1017.

Grid ID	Nom. Re_τ	$N_x \times N_y \times N_z$	Grid points (millions)	Δx^+_{wall}	Δx^+_{cen}	Δz^+_{wall}	Δz^+_{cen}
SG-A	590	$75 \times 153 \times 75$	0.86	50.0	50.0	25	25
SG-B	590	$149 \times 153 \times 149$	3.40	25.0	25.0	12.5	12.5
SG-C	1017	$261 \times 264 \times 261$	17.98	25.0	25.0	12.5	12.5
SG-X	1017	$297 \times 301 \times 297$	26.55	21.6	21.6	10.8	10.8
MG-A	590	see Figure 1	3.63	25.0	25.7	12.5	12.9
MG-B	590	see Figure 1	3.09	25.0	30.9	12.5	15.4
MG-C	590	see Figure 1	2.33	25.0	50.0	12.5	25.0
MG-D	590	see Figure 1	9.27	12.5	25.0	25.0	50.0
MG-E	1017	see Figure 8	14.93	21.6	66.6	10.8	33.3
DNS [5]	590	$384 \times 257 \times 384$	37.90	9.7	9.7	4.8	4.8

Note: x, streamwise direction; y, wall-normal direction; z, spanwise direction.

4.1.1. $Re_\tau = 590$. The first channel-flow simulated here was the $Re_\tau = 590$ case ($Re_m = 21\,870$ based on the bulk mean velocity and channel height 2δ). Some parameters associated with the various grids used in the channel-flow simulations are given in Table I. For all cases shown in this table, the streamwise and spanwise extents of the physical domain were taken to be $2\pi\delta$ and $\pi\delta$, respectively. Grids SG-A and SG-B represent single-grid topologies of various streamwise and spanwise resolutions. Grids MG-A through MG-D represent multiple-grid topologies formed by splitting the height of the channel into four equal (in terms of the number of wall-normal grid points) grids with varying streamwise and spanwise resolutions. The dimensions of the individual multiple-grid cases as well as close-up views of the overlap regions for each case are given in Figure 1. Grids MG-A through MG-C correspond to a multiple-grid version of SG-B, with less resolution in both streamwise and spanwise directions in the two grids that make up the centre of the channel. In these cases, the volume ratios in the overlap region between the wall grid and the centre grid are approximately 1.05, 1.5, and 4.0, respectively. Grid MG-D is a more-resolved version of Grid MG-C, with double the resolution in both streamwise and spanwise directions but still with a volume ratio of 4.0 in the overlap region. In all grids used at this Reynolds number, the grid-point distribution in the wall-normal direction is the same with a total of 153 grid points utilized across the channel height. The grid is clustered near the wall, with 12 grid points located below $\Delta y^+ = 10$, and minimum and maximum values of Δy^+ given by 0.7 and 17.6 at the wall and in the centre of the channel, respectively. For the multiple-grid cases, the interface between the wall grids and the centre grids is located approximately 102 wall units away from the top and bottom walls. This location for the boundary was chosen in a somewhat *ad hoc* manner to completely contain the peaks in the velocity fluctuation profiles in the near-wall grid, while transitioning to the coarser centre grid quickly to maximize gridpoint savings. No-slip and isothermal boundary conditions are enforced at the upper and lower surfaces along with a zero pressure gradient condition implemented using fourth-order finite differences. Periodic boundary conditions are utilized in both the streamwise and spanwise directions and a source term is added to the x-momentum and energy equations to account for the constant pressure gradient driving the flow [33]. The flowfield was initialized by interpolating previous single-grid solutions at this Reynolds number onto the particular grid. The solutions were advanced between 5000 and 20 000 time steps depending on the case in order to remove any transients, and then statistics were collected for an additional 20 000 time steps. The results shown here were obtained with a time

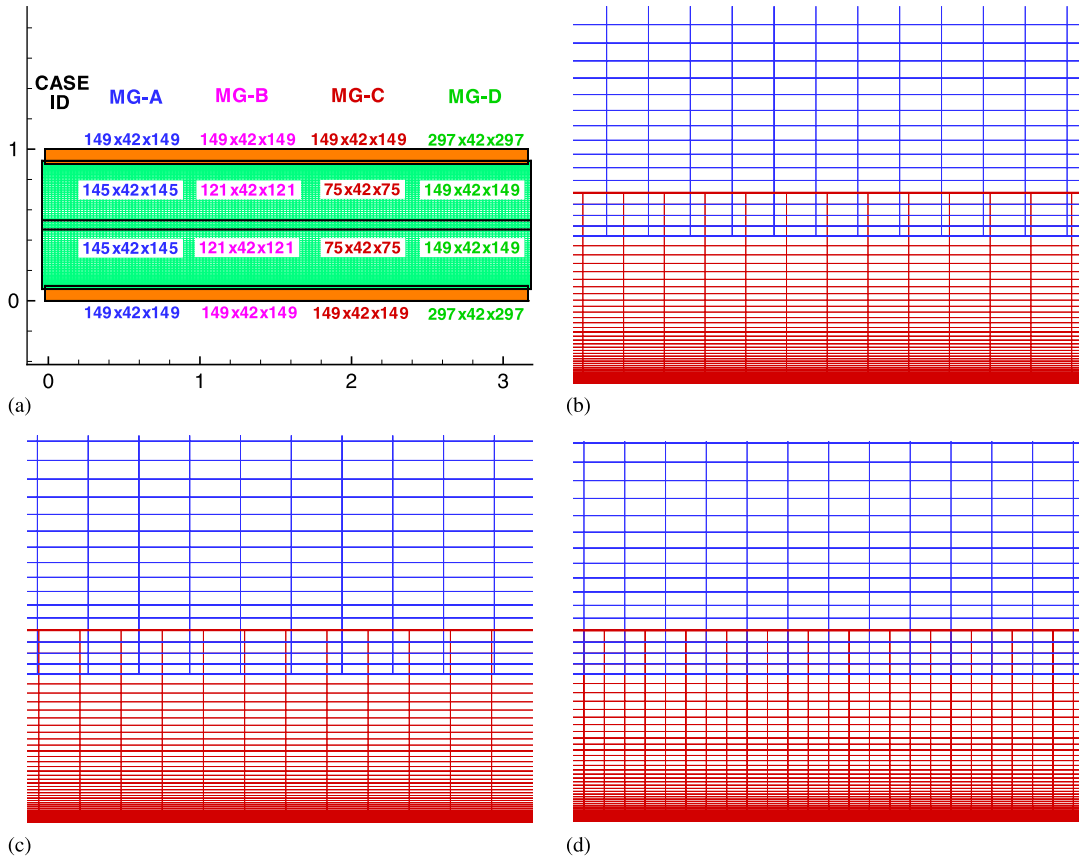

Figure 1. Grid-related data for channel-flow simulations at $Re_\tau = 590$: (a) mesh topology and grid parameters (streamwise × wall-normal × spanwise dimensions); (b) close-up of overlap region for MG-A (volume ratio = 1.05); (c) close-up of overlap region for MG-B (volume ratio = 1.5); and (d) close-up of overlap region for MG-C and MG-D (volume ratio = 4.0).

step of $\Delta t = 0.001$, and some cases were also computed with a time step of $\Delta t = 0.0005$ to verify time-step independence of the final solutions. The specific spatial algorithm employed was the sixth-order accurate spatial discretization with the tenth-order interior filter, and a filter coefficient of $\alpha_f = 0.49$. Results are compared to the benchmark numerical DNS data of Moser *et al.* [5].

The mean streamwise velocity profile, root-mean-squared (rms) velocity fluctuations and Reynolds stresses are plotted over half the channel width in Figures 2–5 for various combinations of single- and multiple-grid systems. Figure 2, which compares the multiple-grid cases MG-A and MG-B to the baseline single-grid case SG-B, demonstrates the impact that the order-of-accuracy of the interpolation procedure has on the accuracy of the velocity fluctuation profiles. A large discrepancy in the profiles, particularly for u^+_{rms} and v^+_{rms}, is observed in the neighbourhood of the grid interface when using standard second-order interpolation. However, the use of sixth-order interpolation produces a smooth transition between grids and results that very closely match the

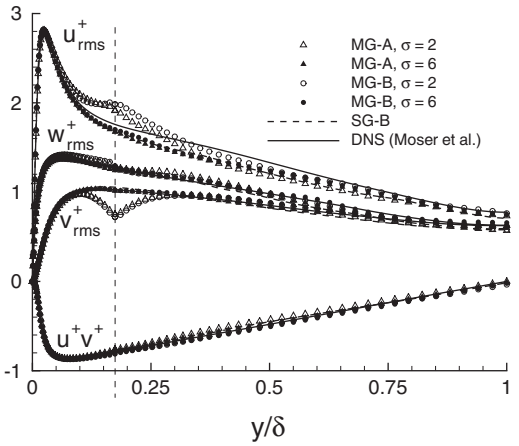

Figure 2. Fluctuating velocity profiles for channel flow at $Re_\tau = 590$, grids MG-A, MG-B and SG-B (dashed lines represents grid interfaces).

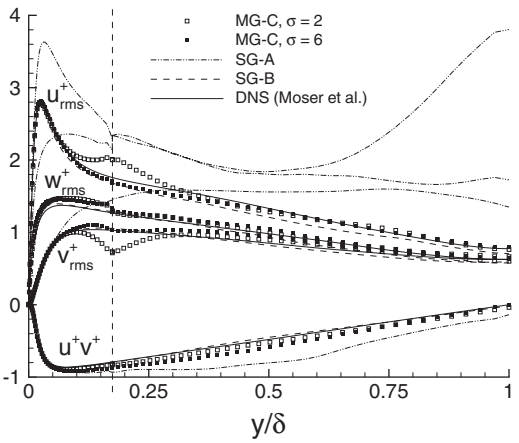

Figure 3. Fluctuating velocity profiles for channel flow at $Re_\tau = 590$, grids MG-C, SG-A and MG-B.

baseline single-grid case. The errors associated with the second-order interpolation are present in case MG-A, despite the fact that the volume ratio between grids in this case is nearly unity. Thus, this error is associated with the interpolation process itself and is not directly related to the disparity in cell size in the overlap region.

In Figure 3, the velocity fluctuations and Reynolds stress for grid MG-C, with a volume ratio of 4.0 in the overlap regions, are plotted and compared with both the baseline single grid system SG-B and the coarse single-grid system SG-A. Grid system SG-A represents the single-grid system possessing the same streamwise and spanwise resolution throughout the channel as the multi-grid case MG-C has on the interior of the channel. It is clear that this reduced global resolution is inadequate to capture the turbulent scales present at the current Reynolds number. The presence of

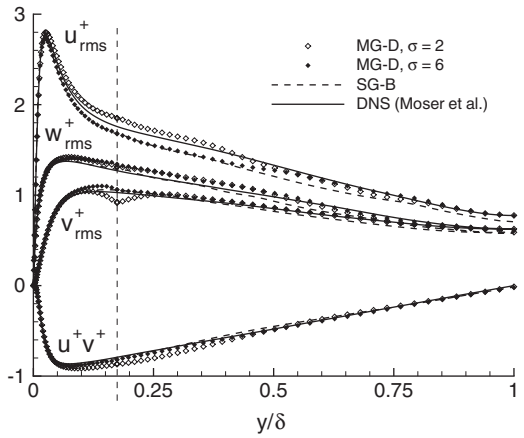

Figure 4. Fluctuating velocity profiles for channel flow at $Re_\tau = 590$, grids MG-D and SG-B.

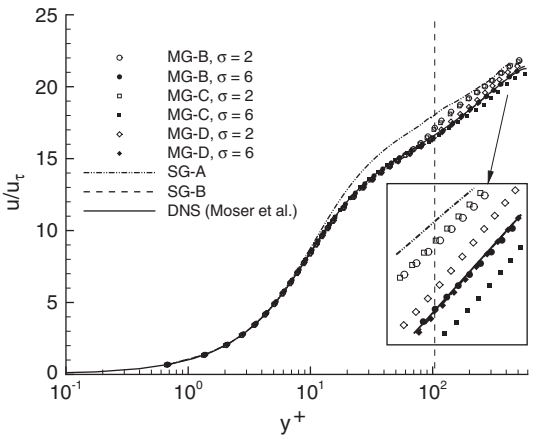

Figure 5. Mean streamwise velocity profile for channel flow at $Re_\tau = 590$.

the computational boundaries are also evident in SG-A due to the coarseness of the grid, despite the fact that the overlap regions consist solely of coincident points. However, grid MG-C, with identical resolution as SG-A in the centre of the channel and improved resolution near the wall, produces velocity fluctuation profiles that match the single-grid results of SG-B well when using sixth-order interpolation. The second-order interpolation performs poorly for overset-grid system MG-C with large jumps occurring in the u^+_{rms} and v^+_{rms} profiles as they cross the grid interface. For this relatively large volume ratio, there is some differences observed in the v^+_{rms} and w^+_{rms} profiles near the wall and in the grid-interface region when compared to the single-grid and DNS results, even when using the sixth-order interpolation. Also, the Reynolds stress profile deviates more from the single-grid solution for the $\sigma = 6$ case than for the $\sigma = 2$ case.

To determine if this behaviour is caused by the large discrepancy in cell size in the overlap region between grids or if this is a resolution effect, a multiple-grid topology with twice the resolution of case MG-C in the streamwise and spanwise directions was developed. The fluctuating velocity and Reynolds stress profiles for this topology (MG-D) are shown in Figure 4. A marked improvement in agreement between the multiple-grid, $\sigma = 6$ case and the single-grid and DNS results is observed, although slight overshoots in the v^+_{rms} and w^+_{rms} profiles are still present. While the second-order interpolation results are also better on this more-refined grid compared with the previous coarser grid results, they still exhibit additional error compared to the results obtained with high-order interpolation. Thus, the errors present in the MG-C case appear to be caused by a lack of resolution in the interior of the channel rather than due to the volume ratio of 4.0 in the overlap region. This is consistent with the findings in Reference [16], where volume ratios of up to 16 were utilized with no detrimental effect as long as the grid resolution of the coarser grid was sufficient to resolve the flow features.

The mean streamwise velocity profiles for the two single-grid cases as well as multiple-grid topologies MG-B, MG-C and MG-D are shown in Figure 5. The profile obtained with SG-B matches the DNS results extremely well, as was also seen in a previous study using the single-block algorithm at this Reynolds number [18]. The profile obtained with MG-B using the sixth-order interpolation also agrees with the single-grid ILES and DNS results very well, but using second-order interpolation on the same grid causes a noticeable deviation even at this small volume ratio. Differences between the DNS/single-grid profile and those obtained with MG-C are observed for both $\sigma = 2$ and 6. However, increasing the resolution (Case MG-D) results in the profile obtained with sixth-order interpolation collapsing onto the single-grid/DNS profile, while the second-order interpolation still exhibits some error. Table II compiles the absolute per cent differences between the various grid systems and interpolation orders in a more quantitative manner, comparing the mean streamwise velocity at the point $y^+ = 175$ to the 'exact' value as given by the DNS solution. One-dimensional streamwise energy spectra are shown in Figure 6 for two locations in the channel; well within the boundary layer at $y^+ \approx 5.4$ and ≈ 590, the centre of the channel. Results from the single-grid system SG-B as well as the multiple-grid system MG-C are compared to the well-resolved DNS data. The spectra near the wall shows that energy-containing scales are resolved throughout much of the inertial region for both the single-grid and multiple-grid ILES computations, although the current computations are not resolving scales at the smallest wave numbers that are

Table II. Absolute per cent difference in mean streamwise velocity values at $y^+ = 175$ between various grid systems/orders of interpolation and DNS solution, $Re_\tau = 590$.

Grid ID	σ	$u/u_\tau(y^+ = 175)$	Absolute % difference from DNS
DNS	—	18.00	—
SG-A	—	19.23	6.8
SG-B	—	17.93	0.4
MG-B	2	18.86	4.8
MG-B	6	17.99	<0.1
MG-C	2	18.84	4.6
MG-C	6	17.76	1.4
MG-D	2	18.22	1.2
MG-D	6	17.91	0.5

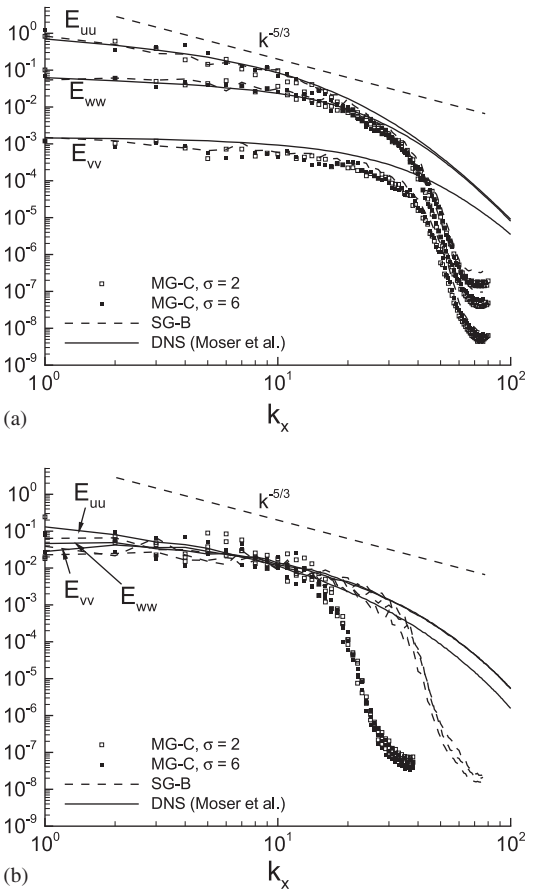

Figure 6. Streamwise one-dimensional energy spectra for channel-flow simulations at $Re_\tau = 590$: (a) $y^+ \approx 5.4$ and (b) $y^+ \approx 590$.

being captured by the DNS. The effect of the coarser resolution in the streamwise direction in the multiple-grid topologies is clearly seen in the spectra at $y^+ \approx 590$, as the wave number at which the MG-C computations matches the single-grid and DNS data shifts considerably to the left. However, this lack of resolution in the centre of the channel has a minimal effect on the mean velocity and first-order turbulent statistics considered here. Only seemingly minor changes are observed for the different values of σ on the multiple-grid topologies. Although not shown here, the one-dimensional spanwise energy spectra displays similar behaviour as that in the streamwise direction. Contours of the instantaneous streamwise velocity component obtained using MG-C with $\sigma = 6$ are shown in Figure 7 for three planes ($x = 0$, $z = 0$, $y^+ \approx 5.4$) and show the low-speed streaks near the wall and the nature of the turbulent structures at this Reynolds number.

4.1.2. $Re_\tau = 1017$. The second channel flow considered here is at $Re_\tau = 1017$ ($Re_m = 45\,552$) with M_∞ again set to 0.1. This case has been previously examined computationally by Kravchenko [6]

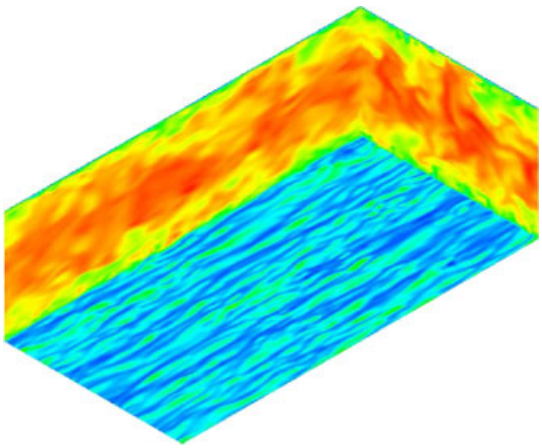

Figure 7. Instantaneous streamwise velocity contours for channel flow at $Re_\tau = 590$, grid MG-C.

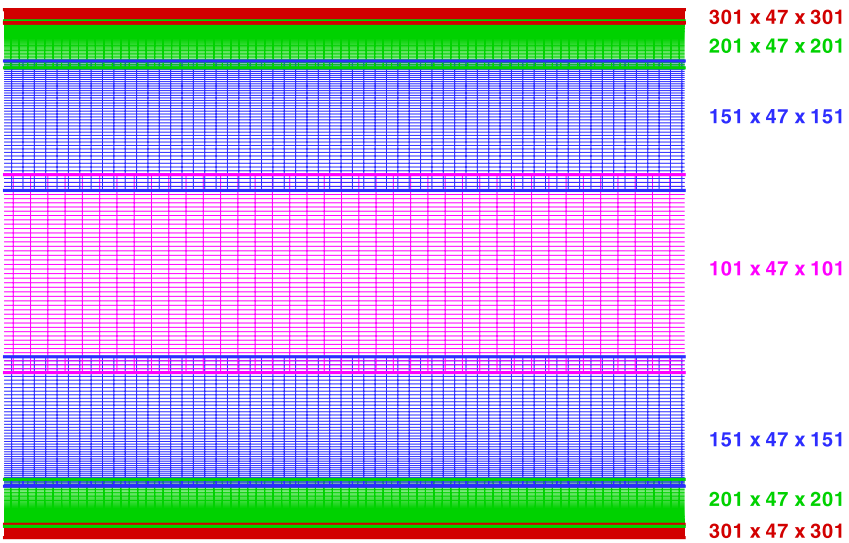

Figure 8. Grid topology for multiple-grid channel flow simulation at $Re_\tau = 1017$, every other gridline removed for clarity (streamwise × wall-normal × spanwise dimensions).

and has corresponding experimental data collected by Wei and Willmarth [34]. Two grids were employed here and are detailed in Table I. Grid SG-C is a single-grid system that was developed by increasing the number of grid points to maintain the same resolution as grid SG-B had for the $Re_\tau = 590$ case ($\Delta y^+_{\text{wall}} = 0.7$ and $\Delta y^+_{\text{cen}} = 17.6$). Grid MG-E is a multiple-grid topology consisting of seven grids of varying streamwise and spanwise resolutions as shown in Figure 8 with interfaces

located at approximately 51, 241 and 700 wall units from the top and bottom walls of the channel. As was the case in the previous channel computation, the exact location of the first grid boundary off of the wall was determined by the location of the peaks in the velocity fluctuation profiles for the single-grid calculation, while subsequent boundaries were determined by considerations involving the wall-normal stretching ratios and volume ratios in the grid overlap regions. The wall-normal grid spacing in this case was decreased slightly with $\Delta y^+_{\text{wall}} = 0.5$ and Δy^+_{cen} remaining 17.6. The volume ratios between grids in the overlap region are 2.25, $1.\bar{7}$, and 2.25 from wall to channel centre, respectively. Finally, Grid SG-X is a fictitious case that represents a single-grid topology using the resolution of the wall grid from case MG-E. While this case was not run here, it serves as a reference for evaluating the savings in grid points when utilizing the multiple-grid systems. The use of the multiple-grid topology MG-E results in 45% fewer grid points than for this single-grid case, in spite of the fact that they have identical near-wall resolution.

Identical boundary conditions as employed in the previous channel study were again used, and the Beam-Warming time-integration method with a value of $\Delta t = 0.00025$ was utilized for both single- and multiple-grid systems. The same spatially sixth-order differencing/tenth-order filtering algorithm as the previous problem was also employed. The calculation was initiated by interpolating the flowfield from the $Re_\tau = 590$ case onto SG-C and then running the solver for 20 000 time steps to allow for the new flow to develop. Statistics were then collected for an additional 20 000 time steps. For the multiple-grid case, the single-grid flowfield from case SG-C was interpolated onto MG-E and the solution was advanced 5000 time steps to allow the new flowfield to develop. Statistics were then collected over an additional 20 000 time steps. The results for the mean streamwise velocity profile and velocity fluctuations are given in Figures 9 and 10 and compared to the existing experimental data [34] and to previous computations using a B-spline/spectral algorithm [6]. The mean streamwise velocity profiles are also compared to the 'law of the wall' as plotted in [34]. The agreement between the current computations and previous theoretical, experimental and computational data is very good, with the per cent difference at the centre of the channel between the current computation and experimental data equal to 6.7% for the single-grid case and 1.7% for the multiple-grid case. The better agreement for the multiple-grid case, with its coarser resolution in the centre region, could be a product of its superior near-wall

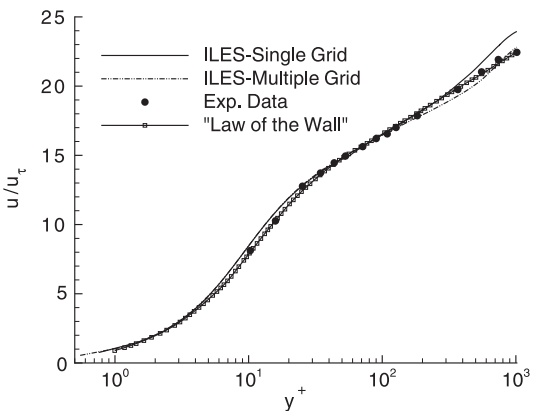

Figure 9. Mean streamwise velocity profile for channel flow at $Re_\tau = 1017$.

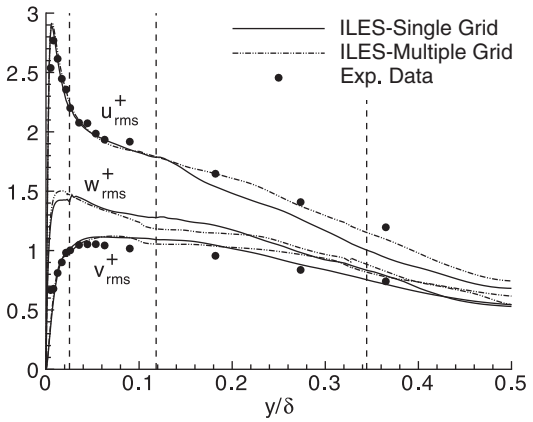

Figure 10. Fluctuating velocity profiles for channel flow at $Re_\tau = 1017$.

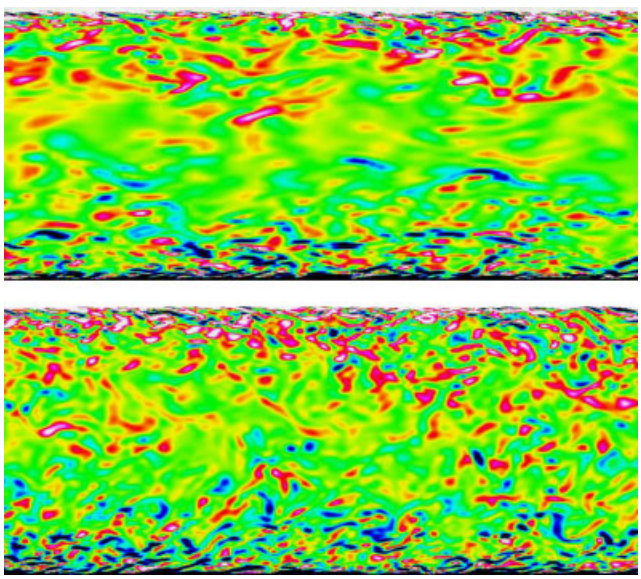

Figure 11. Comparison of instantaneous mid-span z-component of vorticity between single-grid (bottom) and multiple-grid (top) computations for channel-flow simulations at $Re_\tau = 1017$.

resolution compared to the single-grid case or it could be fortuitous. The rms-velocity fluctuation profiles shown in Figure 10 are also seen to be in good agreement with existing data. The slight over-prediction of the peak in the streamwise fluctuating velocity would indicate that the near-wall region is still slightly under-resolved. Turbulent structures and the effect of the varying grid resolution across the channel height are visualized in Figure 11, which shows the contours of z-vorticity magnitude at the mid-span for both single- and multiple-grid topologies. The fine-scale structure present near the top and bottom walls is visible in both cases. However, the decrease

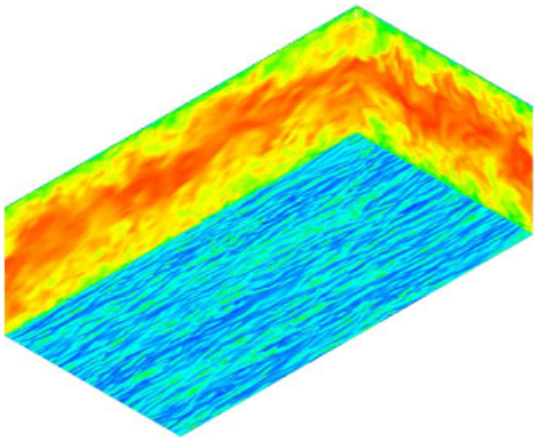

Figure 12. Instantaneous streamwise velocity contours for channel flow at $Re_\tau = 1017$, grid MG-E.

in resolution at the centre of the channel is clearly visible in the multiple-grid case through the loss of the fine-scale structure compare to the single-grid case. While it would be detrimental if it occurred near the wall where the turbulent production is high, this loss of fine-scale structure in the centre of the channel again has a minimal impact on the mean velocity and first-order statistics. Contours of the instantaneous streamwise velocity component obtained with MG-E are given in Figure 12 for three planes ($x = 0$, $z = 0$, $y^+ \approx 5.4$) and show the finer scales present at this Reynolds number when compared with the $Re_\tau = 590$ case from Figure 7.

4.2. Turbulent flow over single circular cylinder

The final problem examined here is the transitional flow over a single circular cylinder at $Re_D = 3900$ and $M_\infty = 0.1$. This case has been previously studied both experimentally and computationally (see Kravchenko and Moin [35] and references therein), and has proved to be a challenging problem due to the transitional nature of the flow at this Reynolds number. This problem has also been studied with a single-grid vector version of the current high-order spatial differencing/filtering algorithm [33], and a parallel, single-grid version of the algorithm with coincident grid points in all overlap regions [3]. With the development of the capability for the current high-order algorithm to handle holes and maintain high-order accuracy at interpolation boundaries, multiple-grid studies were conducted to investigate the flexibility of the overset-grid method in reducing the number of grid points through the use of selective grid refinement in critical areas.

The multiple-grid topology used in this study is shown in Figure 13 and consists of four grids: a body-fitted grid around the surface of the cylinder (dimensioned $199 \times 61 \times 45$); a near-field polar grid ($201 \times 71 \times 45$); a fine wake grid downstream of the cylinder ($248 \times 101 \times 45$); and a background farfield grid ($91 \times 91 \times 45$). The total number of grid points for the overset-grid system is thus 2.92 million. The cylinder surface is located at $r/D = 0.5$, while the outer interpolated boundary of the body-fitted grid is found at $r/D = 1.625$. The body-fitted grid has uniform azimuthal spacing on the front ($\Delta\theta = 3.07°$) and rear ($\Delta\theta = 1.25°$) faces of the cylinder, with stretched transitional regions at $\theta = 90°$ and $270°$ to smoothly switch from one spacing to the other. The radial spacing for the body-fitted grid was equal to 0.001 at the wall and was stretched

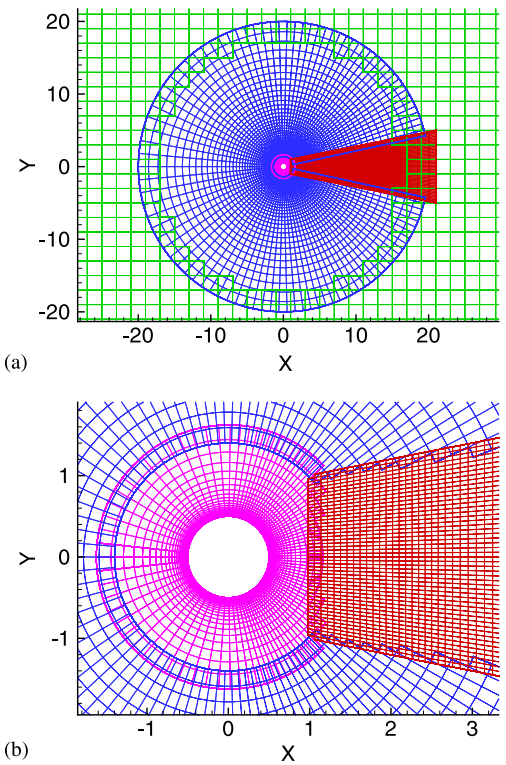

Figure 13. Multiple-grid topology for transitional flow over circular cylinder, every other grid line removed for clarity: (a) all four grids of multiple-grid system and (b) close-up of body-fitted grid and wake grid.

using a hyperbolic stretching function to 0.095 at its outer boundary. The farfield boundaries are located at $x = \pm 100$, $y = \pm 100$, and the length of the computational domain in the spanwise direction was approximately $\pi D/2$. For comparison purposes, the coarse single-grid (SG-C) and fine single-grid (SG-F) topologies from [3] had 1.9 and 11.9 million grid points, respectively. The spatial algorithm employed in this case is again sixth-order differencing/tenth-order filtering, with a filter coefficient of $\alpha_f = 0.45$ and sixth-order interpolation at all interpolated boundaries. The boundary conditions used at the solid surface of the cylinder include no-slip and isothermal wall conditions as well as a zero pressure gradient condition implemented using fourth-order finite differences. Periodic boundary conditions were enforced at the spanwise boundaries as well as at the azimuthal overlap in the body-fitted O-grid. At the downstream farfield boundary, first-order extrapolation coupled with rapid grid-stretching was used to convect the flow out of the computational domain, while the top, bottom, and upstream farfield boundaries were set using free-stream conditions. The computation was initialized by interpolating an existing single-grid solution onto the topology shown in Figure 13 and allowing the computation to advance 20 000 time steps to remove any grid-related start-up transients. Statistics were then collected for an additional 60 000 time steps. The Δt used for all results shown here was 0.002. Experimental data used for comparison were taken from Reference [35].

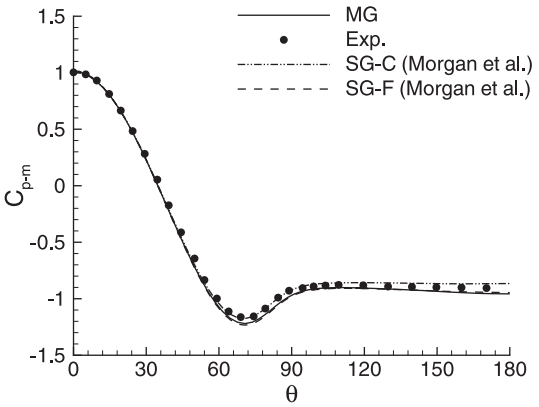

Figure 14. Mean C_p as a function of θ on surface of cylinder, $Re_D = 3900$.

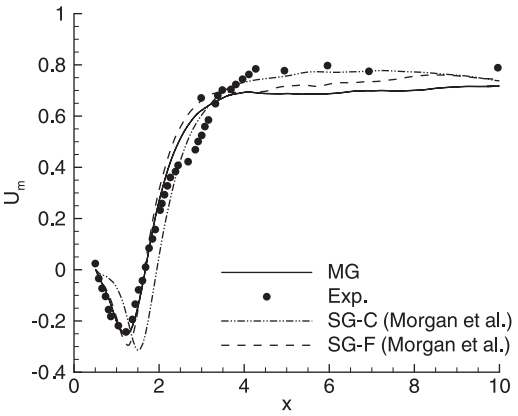

Figure 15. Spanwise-averaged mean streamwise velocity component along wake centreline of cylinder, $Re_D = 3900$.

The mean pressure coefficient along the surface of the cylinder and the mean streamwise velocity component along the wake centreline are shown in Figures 14 and 15, respectively. The pressure coefficient profile for the multiple-grid case is nearly identical to that which was obtained using the fine single-grid topology. However, the location and magnitude of the minimum point in the mean streamwise velocity profile match the experimental data much better than either single-grid system. All the numerical results shown here exhibit some discrepancy with the experimental results in the region $2<x<4$. This discrepancy was also observed in the numerical results in Reference [35] and was attributed to 'early transition in the separating shear layers which affect the size of the recirculating region' [35]. The mean streamwise and vertical velocity component profiles are shown at various stations downstream from the cylinder in Figures 16 and 17 and in general show good agreement with the fine single-grid case in spite of having only one-fourth of the number of grid points. Of particular interest is the ability of the multiple-grid topology to capture

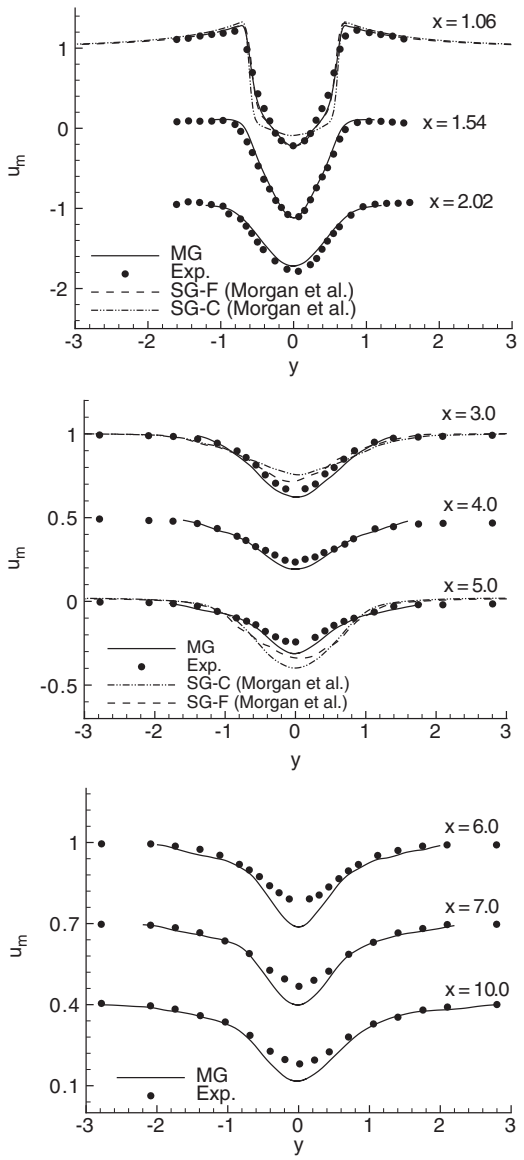

Figure 16. Spanwise-averaged mean streamwise velocity distributions in wake of cylinder, $Re_D = 3900$.

the 'V'-shaped profile of the mean streamwise velocity immediately downstream of the cylinder as is seen in this set of experimental data. The velocity fluctuation profiles and Reynolds stress profiles downstream of the cylinder are shown in Figures 18–20 and also show good agreement with the previous fine-grid results. In general, the accuracy of the computational results compared to the experimental data degrades as the distance from the cylinder increases. This is thought to be caused by insufficient domain size in the spanwise direction, which is constraining the development

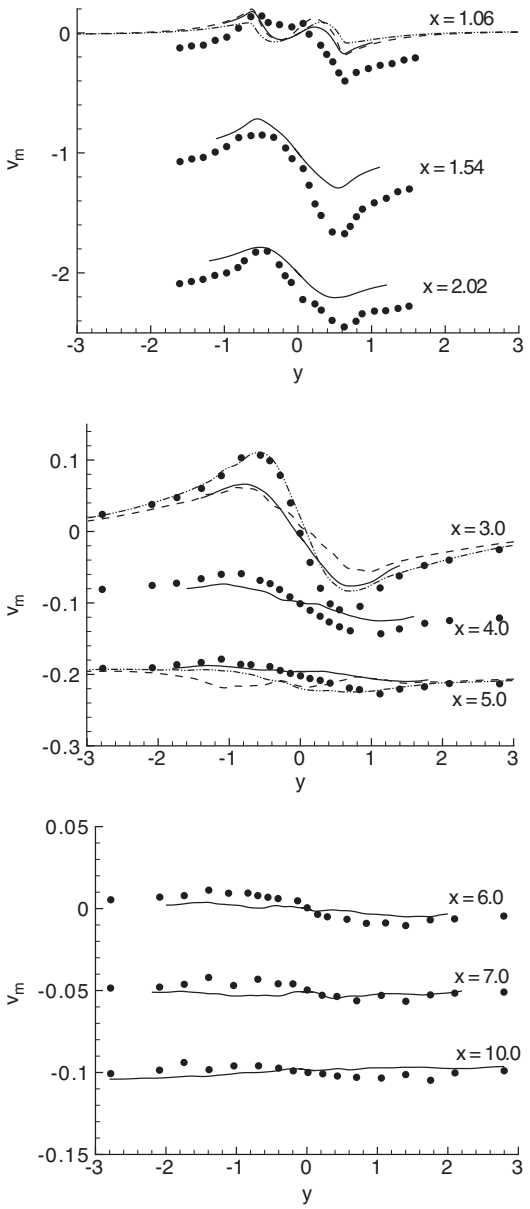

Figure 17. Spanwise-averaged mean crossflow velocity distributions in wake of cylinder, $Re_D = 3900$ (see Figure 16 for legend).

of the larger spanwise structures that form downstream [35]. The normalized frequency spectra of the crossflow velocity at three stations downstream of the wake match very well with the experimental spectra, including capturing the location and magnitudes of both the primary and

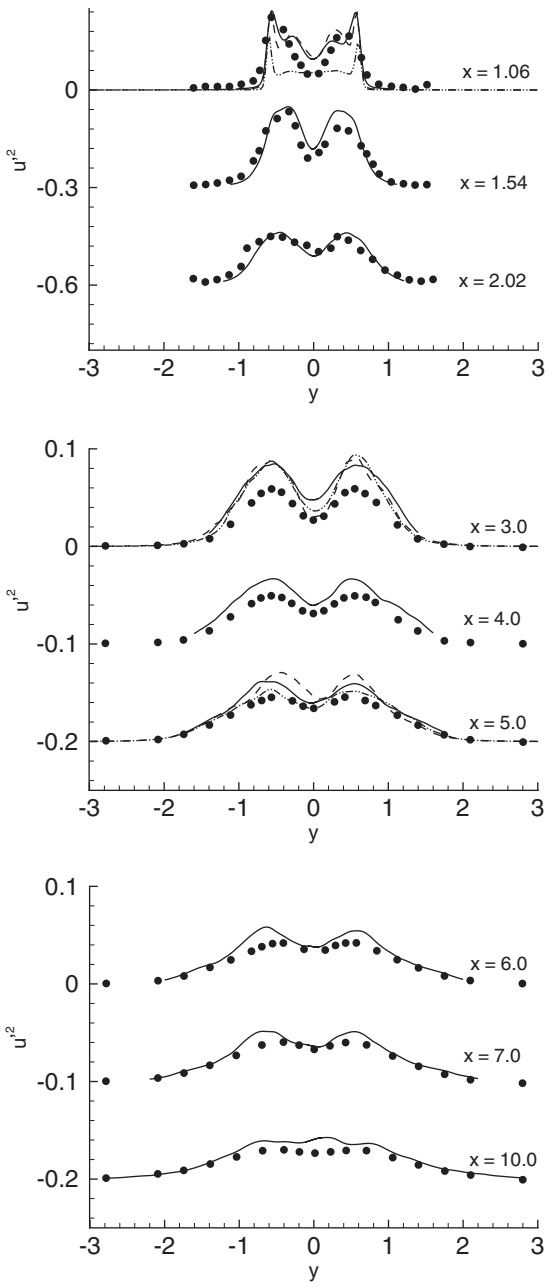

Figure 18. Spanwise-averaged streamwise velocity fluctuation profiles in wake of cylinder, $Re_D = 3900$ (see Figure 16 for legend).

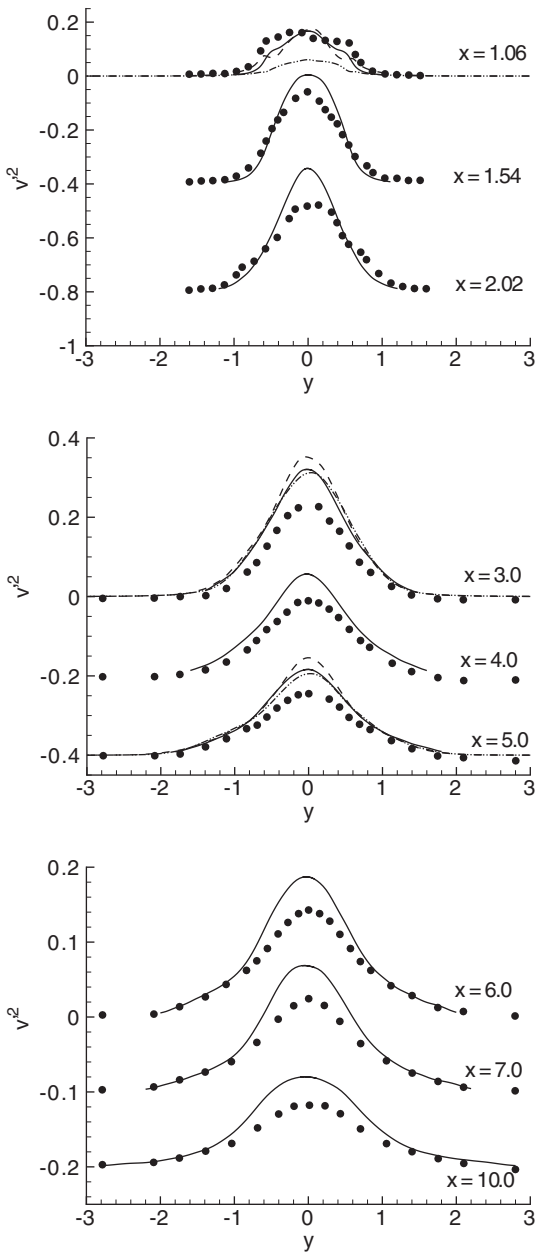

Figure 19. Spanwise-averaged crossflow velocity fluctuation profiles in wake of cylinder, $Re_D = 3900$ (see Figure 16 for legend).

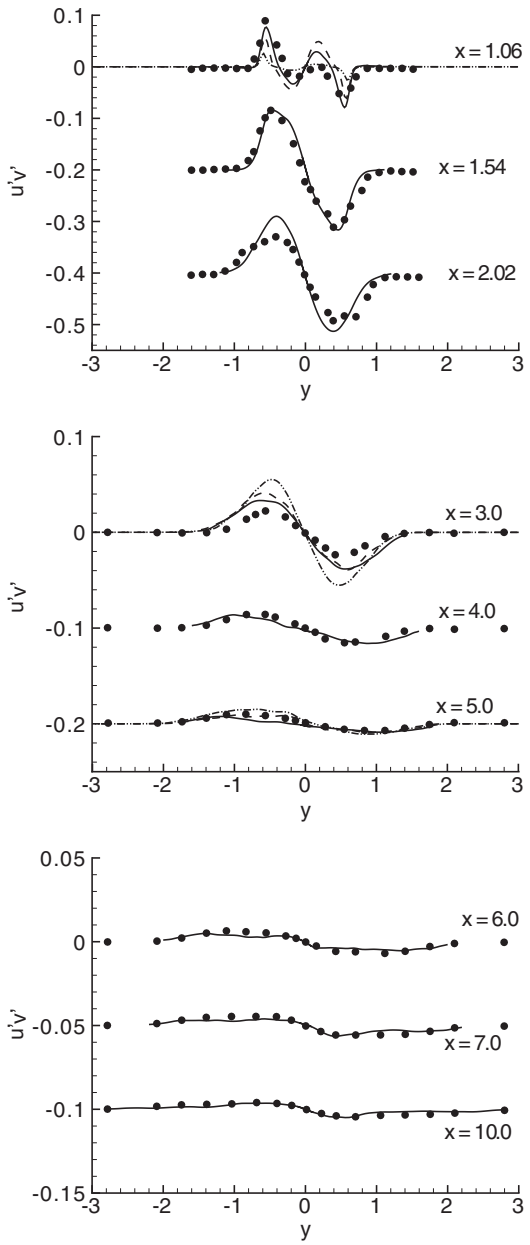

Figure 20. Spanwise-averaged Reynolds stress profiles in wake of cylinder, $Re_D = 3900$ (see Figure 16 for legend).

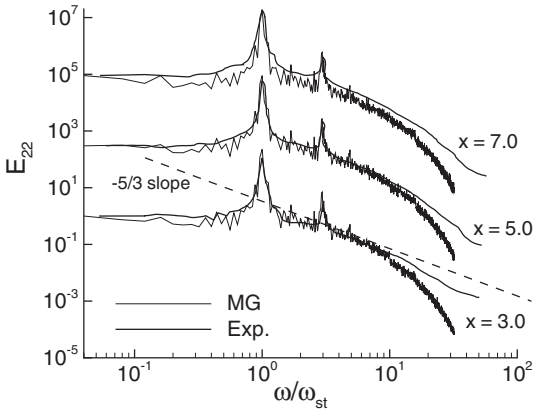

Figure 21. Spanwise-averaged crossflow velocity frequency spectra at stations in cylinder wake, $Re_D = 3900$.

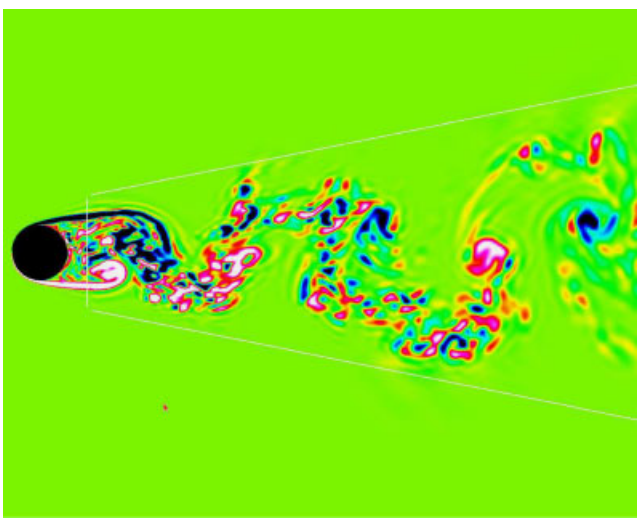

Figure 22. Instantaneous mid-span z-vorticity contours in near-wake ($x \leqslant 11$) region of circular cylinder, $Re_D = 3900$ (white line indicates boundary of wake grid).

secondary shedding frequencies (Figure 21). Instantaneous vorticity contours along the midspan plane shown in Figure 22 capture several large-scale vortical structures and demonstrate the ability of the refined wake grid to resolve the fine scales present in the larger structures.

5. CONCLUSION

A high-order overset-grid approach to numerically model turbulent flow problems on general curvilinear grids using large-eddy simulation has been validated by solving the benchmark problems

of fully developed turbulent channel flow at various Reynolds numbers and flow over a single circular cylinder with a transitional wake. The ability of the current algorithm to employ high-order interpolation at overset boundaries and to deal with holes cut into grids greatly adds to the flexibility of the overall high-order approach. Volume ratios between overlapping grids of up to 4.0 were employed successfully in the channel problem providing that the resolution on the coarser grid is still adequate to capture the important flow scales. It was also demonstrated using this problem that the current high-order interpolation can have a significant effect on reducing interpolation error at grid boundaries, and that lack of grid resolution, and not grid volume differences in the overlap region, is the primary source of error. Through the use of this technology, grids can be constructed with the gridpoint distribution tailored for the particular problem being studied. Examples shown in this work include the use of nested grids with increased streamwise and spanwise resolution near the solid walls in channel flow, and highly resolved grids in the downstream wake region of the cylinder. Such use of overset grids to provide grid refinement in critical regions of the flow was shown to result in substantial decreases in the number of gridpoints used compared to a single-grid topologies, with nearly a factor of two reduction for the channel-flow problem at $Re_\tau = 1017$, and nearly a factor of four for the circular cylinder problem. The coupling of high-order numerical algorithms and overset-grid techniques continues to show great promise for solving both more geometrically complex as well as more physically realistic problems using current computational resources.

ACKNOWLEDGEMENTS

The authors are grateful for AFOSR sponsorship under a task monitored by Dr T. Buetner. This work was also supported by a grant of HPC time from the DoD HPC Shared Resource Centers at Aeronautical Systems Center, Wright-Patterson AFB, Ohio.

REFERENCES

1. Visbal MR, Rizzetta DP. Large-eddy simulation on curvilinear grids using compact differencing and filtering schemes. *Journal of Fluids Engineering* (ASME) 2002; **124**(4):836–847.
2. Rizzetta DP, Visbal MR. Large-eddy simulation of supersonic cavity flowfields including flow control. *AIAA Journal* 2003; **41**(8):1452–1462.
3. Morgan PE, Visbal MR, Rizzetta DP. A parallel high-order flow solver for large-eddy and direct numerical simulation. *Thirty-second Fluid Dynamics Meeting*, AIAA Paper 2002-3123, St. Louis, MO, June 2002.
4. Kim J, Moin P, Moser RD. Turbulence statistics in fully developed channel flow at low Reynolds numbers. *Journal of Fluid Mechanics* 1987; **177**:133–166.
5. Moser RD, Kim J, Mansour NN. Direct numerical simulation of turbulent channel flow up to $Re_\tau = 590$. *Physics of Fluids* 1999; **11**4:943–945.
6. Kravchenko AG, Moin P, Moser RD. Zonal embedded grids for numerical simulations of wall-bounded turbulent flows. *Journal of Computational Physics* 1996; **127**(2):412–423.
7. Morinishi Y, Tamano S, Nakabayashi K. A DNS algorithm using B-spline collocation method for compressible turbulent channel flow. *Computers and Fluids* 2003; **32**(5):751–776.
8. Giannakouros J, Karniadakis GE. Spectral element-FCT method for scaler hyperbolic conservation laws. *International Journal for Numerical Methods in Fluids* 2005; **14**(6):707–727.
9. Wang ZJ, Zhang L, Liu Y. Spectral (finite) volume method for conservation laws on unstructured grids IV: extension to two-dimensional systems. *Journal of Computational Physics* 2004; **194**(2):716–741.
10. Kwok WY, Moser RD, Jiménez J. A critical evaluation of the resolution properties of B-spline and compact finite difference methods. *Journal of Computational Physics* 2001; **174**(2):510–551.
11. Shariff K, Moser RD. Two-dimensional mesh embedding for B-spline methods. *Journal of Computational Physics* 1998; **145**(2):471–488.

12. Steger JL, Dougherty FC, Benek JA. A chimera grid scheme. In *Advances in Grid Generation*, *ASME-FED*, vol. 5, Ghia KN, Ghia U (eds). The American Society of Mechanical Engineers: New York, 1983; 59–69.
13. Visbal MR, Gaitonde DV. On the use of higher-order finite-difference schemes on curvilinear and deforming meshes. *Journal of Computational Physics* 2002; **181**(1):155–185.
14. Visbal MR, Gaitonde DV. High-order accurate methods for complex unsteady subsonic flows. *AIAA Journal* 1999; **37**(10):1231–1239.
15. Gaitonde DV, Visbal MR. Padé-type higher-order boundary filters for the Navier–Stokes equations. *AIAA Journal* 2000; **38**(11):2103–2112.
16. Sherer SE, Scott JN. High-order compact finite-difference methods on general overset grids. *Journal of Computational Physics* 2005; **210**(2):459–496.
17. Gaitonde DV, Visbal MR. High-order schemes for Navier–Stokes equations: algorithm and implementation into FDL3DI. *Technical Report AFRL-VA-WP-TR-1998-3060*, Air Force Research Laboratory, Wright-Patterson AFB, OH.
18. Visbal MR, Morgan PE, Rizzetta DP. An implicit LES approach based on high-order compact differencing and filtering schemes. *Sixteenth Computational Fluid Dynamics Conference*, AIAA Paper 2003-4098, Orlando, FL, June 2003.
19. Stolz S, Adams N. An approximate deconvolution procedure for large-eddy simulation. *Physics of Fluids* 1999; **11**(7):1699–1701.
20. Mathews J, Lechner R, Foysi H, Sesterhenn J, Friedrich R. An explicit filtering method for LES of compressible flows. *Physics of Fluids* 2003; **15**(8):2279–2289.
21. Moin P, Squires W, Cabot W, Lee S. A dynamic subgrid-scale model for compressible turbulence and scalar transport. *Physics of Fluids* 1991; **3**(11):2746–2757.
22. Lele SK. Compact finite difference schemes with spectral-like resolution. *Journal of Computational Physics* 1992; **103**(1):16–42.
23. Sherer SE, Visbal MR. Computational study of acoustic scattering from multiple bodies using a high-order overset grid approach. *Ninth Aeroacoustics Conference*, AIAA Paper 2003-3203, Hilton Head, SC, June 2003.
24. Sherer SE. Further analysis of high-order overset grid method with applications. *Sixteenth Computational Fluid Dynamics Conference*, AIAA Paper 2003-3839, Orlando, FL, June 2003.
25. Morgan PE, Visbal MR. Large-eddy simulation of airfoil flows. *Forty-first Aerospace Sciences Meeting*, AIAA Paper 2003-0777, Reno, NV, January 2003.
26. Suhs NE, Rogers SE, Dietz WE. PEGASUS 5: an automated pre-processor for overset-grid CFD. *Thirty-second Fluid Dynamics Meeting*, AIAA Paper 2002-3186, St. Louis, MO, June 2002.
27. Beam RM, Warming RF. An implicit factored scheme for compressible Navier–Stokes equations. *AIAA Journal* 1978; **16**(4):393–402.
28. Fyfe DJ. Economical evaluation of Runge–Kutta formulae. *Mathematics of Computation* 1966; **20**:392–398.
29. Pulliam TH, Chaussee DS. A diagonal form of an implicit approximate-factorization algorithm. *Journal of Computational Physics* 1981; **29**(2):347–363.
30. Gordnier RE, Visbal MR. Numerical simulation of delta-wing roll. *Thirty-first Aerospace Sciences Meeting*, AIAA Paper 93-0554, Reno, NV, January 1993.
31. Del Álamo JC, Jiménez J, Zandonade P, Moser RD. Scaling of the energy spectra of turbulent channels. *Journal of Fluid Mechanics* 2004; **500**:135–144.
32. Fureby C, Grinstein FF. Large eddy simulation of high-Reynolds-number free and wall-bounded flows. *Journal of Computational Physics* 2002; **181**(1):68–97.
33. Rizzetta DP, Visbal MR, Blaisdell GA. A time-implicit high-order compact differencing and filtering scheme for large-eddy simulation. *International Journal for Numerical Methods in Fluids* 2003; **42**(6):665–693.
34. Wei T, Willmarth WW. Reynolds-number effects on the structure of a turbulent channel flow. *Journal of Fluid Mechanics* 1898; **204**:57–95.
35. Kravchenko AG, Moin P. Numerical studies of flow over a circular cylinder at $Re_D = 3900$. *Physics of Fluids* 2000; **12**(2):403–417.